Suid-Afrikaanse Tydskrif vir Natuurwetenskap en Tegnologie 2022; 41(1):1a-1q
South African Journal for Science and Technology 2022; 41(1):1a-1q
https://doi.org/10.36303/SATNT.2022.41.1.860E

SATNT / SAJST
ISSN: 2222-4173 EISSN: 0254-3486

ORIGINAL RESEARCH

Transparent $MgAl_2O_4$ spinel processing utilising a spark plasma sintering furnace and LiF

F Marais,[1,2] H Potgieter,[1] DJ Whitefield[1]

[1] *University of the Witwatersrand, South Africa*
[2] *TecEx, Melrose Arch, South Africa*
Corresponding author: *DJ Whitefield* ***E-mail:*** *david.whitefield@wits.ac.za*

Transparent polycrystalline magnesium aluminate spinel is a potential candidate for the replacement of the fused silica glass used in the transparent armour and windows of spacecraft. This material is less expensive than other viable materials and is thought to have better transparency.

A single-stage spark plasma sintering (SPS) process was used, in conjunction with LiF as a sintering aid, to manufacture transparent magnesium aluminate spinel. The SPS process was selected for this purpose as it allows for rapid heating and cooling, which may aid in maintaining the small grain size thought to be required for optical transparency.

The spark plasma sintering process used yielded spinel disk samples with an average diameter of 20 mm and acceptable transmittance of ≈72% of the visible spectrum (for samples 3 mm thick), but the mechanical properties were poorer than desired. Of particular concern was the low Weibull modulus of only 3.91.

Keywords: spinel, LiF, spark plasma sintering, transmittance

Deursigtige $MgAl_2O_4$ spinelglas-vervaarding met behulp van 'n enkelfase-vonkplasma-sinteroond (spark plasm sintering furnace) en LiF: Deursigtige polikristallyne magnesiumaluminaat-spinel is 'n potensiële kandidaat vir die vervanging van die saamgesmelte silikaglas wat in die deursigtige vensters van pantser voertuie en van ruimtevaartuie gebruik word. Hierdie materiaal is goedkoper as ander moontlike materiale en is vermoedelik meer deursigtig.

'n Enkelfase-vonkplasmasinteringsproses (spark plasma sintering/SPS process) is gebruik, met die toevoeging van LiF as sinteringshulpmiddel, om deursigtige magnesiumaluminaat-spinel te vervaardig. Die SPS-proses is vir hierdie doel gekies omdat dit vinnige verhitting en afkoeling moontlik maak, wat kan help om die klein korrelgrootte te handhaaf wat vermoedelik vir optiese deursigtigheid nodig is.

Die vonkplasmasinteringsproses wat gebruik is, het sirkelvormige spinel-monsters opgelewer met 'n gemiddelde deursnit van 20 mm en aanvaarbare transmittansie van ≈72% van die sigbare ligspektrum (vir monsters 3 mm dik). Die meganiese eienskappe van die materiaal was egter swakker as verlang. Veral sorgwekkend was die lae Weibull-modulus van slegs 3.91.

Trefwoorde: sinter, LiF, vonkplasmasinteringsproses, deursigtig

Introduction

Polycrystalline magnesium aluminate spinel ($MgAl_2O_4$) has a theoretical transmission range of ~86% to 87% across the visible spectrum (taken here as between 380 nm to 740 nm) (Krell, et al., 2009)(Harris & Turri, 2013). Its high theoretical transmittance, combined with its superior mechanical properties, as compared to silica-glass, makes it an attractive replacement for the use as the strike-face of armoured windows (Straßburger, 2009) and the fused-silica windows used in spacecraft (its thermal and chemical stability add to its appeal in this regard)(Salem, 2013). To attain its theoretical transmittance, the spinel would have to be defect free, which is practically impossible. However, the transmittance can still be high enough for the aforementioned applications if the porosity is extremely low, and there are virtually no secondary phases (Goldstein, 2012).

Magnesium aluminate spinel is an intermediate phase in the $MgO - Al_2O_3$ system. The $MgO - Al_2O_3$ system has very low terminal solubilities, but the solubility of MgO and especially Al_2O_3 in spinel occurs between 40–80 mol % Al_2O_3 at about say 2000°C. When spinel is expressed as $MgO.nAl_2O_3$, the values of n can range from $0.6 < n < 7$ at ~1900°C (Hallstedt, 1992). The conventional unit cell of spinel is Face-Centred Cubic (FCC), with a basis of two formula units (Sickafus & Wills, 1999). In the ideal spinel structure, the anion sublattice is arranged in a pseudo-cubic close packed spatial arrangement of anions that are slightly dilated out of true cubic positions (Ganesh, 2013). The Mg^{2+}-cations occupy 8 of the 64 tetrahedral sites and the Al^{3+}-cations occupy 16 of the 32 octahedral sites within the unit cell formed by the anion spatial arrangement (Smart & Moore, 2005).

Achieving a high in-line transmission is synonymous to achieving a high transparency. For, this, the scattering losses must be low. The scattering of incident light occurs in optically inhomogeneous materials by secondary phases (which include pores) with different refractive indices (Krell, et al., 2009). The

porosity of translucent matter needs to be < 0.01% for the transmittance of visible light to become significant i.e. less porosity implies less scattering of light and hence better light transmittance (Benitez, et al., 2017). This porosity value is generally accepted, however, as the sample thickness increases the transmittance decreases. Thus, thicker samples would require a lower porosity than thinner samples to attain the same transmittance. Fabricating samples without porosity (full dense) and high purity poses a significant production challenge and this is why SPS was the choice of sintering method.

Lithium fluoride is commonly added in amounts of ~0.5–1.5wt.% as a sintering aid when transmittance is of importance (Esposito, et al., 2015). The LiF is added to the starting powders, which are either $MgAl_2O_4$ powder (Reimanis & Kleebe, 2007) or a mixture of Al_2O_3 and MgO powders (Meir, et al., 2008) (Esposito, 2013).

The addition of LiF has been observed to promote the Al_2O_3 + MgO ⟶ $MgAl_2O_4$ reaction, the densification of the spinel and a reduction in carbon contamination (Meir, et al., 2008). Also, it has been reported that the use of LiF as a sintering aid results in spinel which has a substantially higher Al content (Huang & Sun, 1997) (Rozenburg, et al., 2007). The addition of LiF has helped increase the transparency, but this usually comes at the expense of inferior mechanical properties (Cohen, et al., 2018).

The advantage of using a mixture of Al_2O_3 and MgO powders is that they are commercially available with low mean particle sizes (d_{50}s), have narrow particle size distributions, and have a high purity. Also, the formation of spinel from its oxides is accompanied by a volume expansion of 7.67%. This expansion is expected to aid in closing of pores and resulting densification with applied external pressure (Esposito, et al., 2013).

Based on the information above it is clear that the processing of the $MgAl_2O_4$ is not a straightforward matter and is fraught with a number of potential problems, for example porosity, contamination and grain growth. All of these factors reduce transmittance and decrease the mechanical integrity of the parts produced. The SPS processing route chosen in this investigation was specifically aimed to determine the feasibility of this processing route to eliminate these problems or reduce these to an acceptable level to achieve satisfactory transmittance and equivalent mechanical property characteristics.

Material and methods

The powders used were alumina (Krahn Taimicron TM-DAR > 99.99%) and magnesia (Baikowski M30CR > 99.99%). The sintering aid was lithium fluoride (99.98% pure) obtained from Acros Organics. The particle size (d_{50}) of the MgO powder as per supplier specification was 1.4 µm. The Al_2O_3 powder had a particle size range of 0.10~0.30 µm according to the supplier. Particle size analysis (PSA) of the powders was carried out using a Malvern Mastersizer 2000.

The as-supplied oxides were mixed in equal molar amounts (71.8 wt.% Al_2O_3 and 28.2 wt.% MgO) in a 250 ml zirconium oxide milling jar with absolute ethanol (MK CHEMICAL 99%) to make a slurry. The LiF is hygroscopic and was therefore added to the slurry in a glove box under an argon atmosphere. The LiF was added at an amount of 1 wt.%.

Alumina milling balls were added to the 50 g of powder at a weight ratio of 5:1. The mixing of the powders was done with a planetary micro mill for 9 hours and 46 minutes at 110 rpm. The powder and milling balls were dried using a vertical rotary evaporator. The dried powder was sieved through a 125-micron screen.

The powders were sintered using a Spark Plasma Sintering Furnace (FCT HP-D5 Systeme GmbH). Sintering was performed under vacuum with an absolute gas pressure of ≈250Pa. The heating stages of the process used a pulse time of 10 ms with a pause of 5 ms. A powder mass of 5–6 g was used to produce samples with 20 mm in diameter and 5 mm thicknesses. Samples were sintered in a graphite die set, lined with graphite foil to

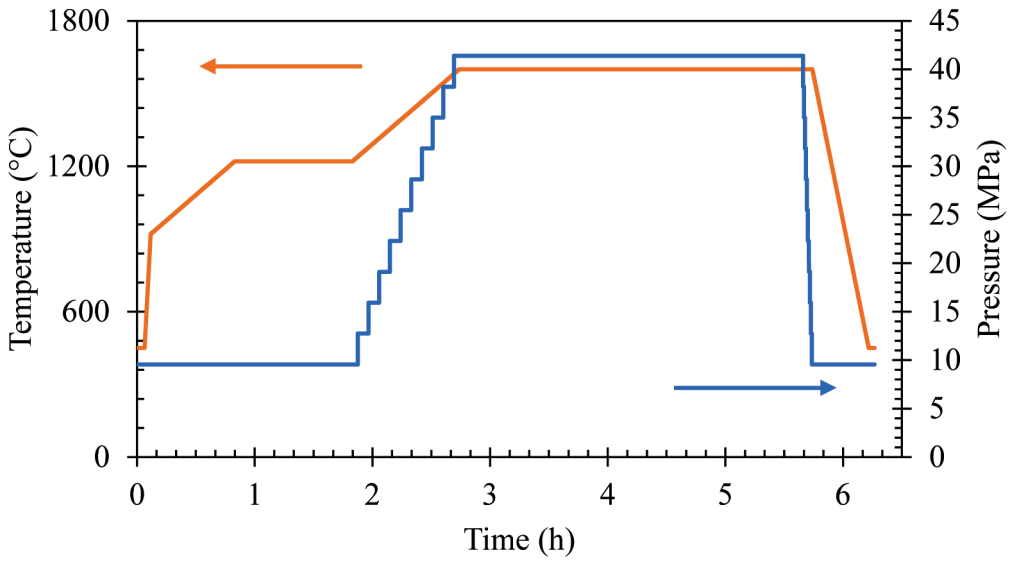

Figure 1: Sintering cycle of the spark plasma sintering furnace

protect the die. During the sintering cycle, the piston movement was recorded to determine the densification behaviour of the powder. This ram piston pressure was limited to 42 MPa. Powder without any LiF addition was also consolidated to determine the influence the LiF had on densification. The thermal expansion of the system was accounted for by doing the sintering cycle without any powder and measuring the piston displacement; this was then used as a baseline for the densification. The sintering profile is shown in Figure 1 and Table 1.

Table I: Sintering cycle of the spark plasma sintering furnace

Temperature (˚C)	Pressure (MPa)	Duration (min)
RT to 450	0 to 10	5
450 to 920	10	3
920 to 1220	10	43
1220	10	60
1220 to 1600	10 to 40	54
1600	40	175
1600	40 to 10	5
1600 to 450	10	29
450 to RT	10	5

The sintered samples were ground from a thickness of ~5 mm to 3 mm. They were then polished to 1 µm finish. Initially polishing was going to be done down to the 0.05-micron slurry; however, this slurry preferentially removed material from the grain boundaries, which resulted in a lower resolution of the light passing through the samples. The Archimedes method was used to determine the density of the polished samples.

The transmission test was done using a UV-Vis-NIR spectrophotometer (Agilent Technologies Cary 5000). The samples were placed at the far end of the sample holder, away from the detector, to ensure that minimal scattered light was detected.

X-Ray diffraction (XRD) analysis was performed using a Bruker D2 instrument. Sintered samples were cut through the centre of the disk then ground and polished. The Co Kα radiation was generated at 10 mA and 30 kV to produce diffractograms over a range of 10 to 90° 2q with a step size of 0.026° 2θ and a scan step time of 3.8 s. These were analysed using EVA© software (Bruker) in conjunction with the International Centre for Diffraction Data (ICDD) database (2019).

A Carl Zeiss Sigma field emission gun scanning electron microscope (FEG-SEM) was used in the characterisation of the powders and the sintered samples. Fracture surfaces were coated with Au and Pd, and aluminium/silver tape was used to ground the fracture surface to the metallic sample holder. Energy Dispersive X-Ray analysis (EDX) was used in conjunction with the SEM analysis to identify the elements present.

A light microscope was used to characterise the grain structure of the sintered samples. Sintered samples were cut and their cross-section polished. These samples were then thermally etched at 1200°C for 30 min. The cross-section of the samples was coated with Au and Pd. The samples were coated, not to enable conductivity, but because they were transparent to visible light. The coating enabled the reflection of the visible light thus illuminating the surface analysed by the optical microscope. Optical microscopy was used in lieu of SEM due to the large grains. The images acquired with the optical microscope were used in conjunction with ImageJ software to measure grain size.

The hardness indents were made using a Leco V-100-A2 Vickers hardness tester with a diamond indenter. A load of 49N (5kgf) was applied and maintained for 30 seconds. The Ball on 3 Balls (B3B) test was used to determine the biaxial flexural strength. A Tinius Olsen Universal Press was used to fracture the samples, along with a positioning aid and four balls.

Results

The measured particle sizes of the powders are given in Table 2. The measured MgO particle size was slightly larger than that stated by the supplier (1.87 µm instead of 1.4 µm). Approximately 77vol.% of the Al_2O_3 powder was within the nominal range of 0.10~0.30 µm, however, ~22vol.% was larger than 0.30 µm. The relatively large d_{90} of the Al_2O_3 powder indicated the presence of agglomeration, which was confirmed by the SEM.

Table II: Characteristic particle sizes for the MgO and Al_2O_3 powders

Powder	d_{10} (µm)	d_{50} (µm)	d_{90} (µm)
Al_2O_3	0.12	0.19	2.58
MgO	1.07	1.87	3.43

Figure 2 shows a FEG-SEM image of the mixed powders. The MgO crystallites (the cubic particles) are smaller than the Al_2O_3 crystallites (rounded particles) within the mixed powder. The scale on which these powders mixed was far smaller than the measured particle sizes. However, there were still aggregates of MgO and Al_2O_3 present, there were very few individual crystallites. EDS (Figure 3) and XRD (Figure 4) confirmed the presence of Mg, Al, O, and MgO and Al_2O_3, respectively. Using the measured Al and Mg atomic mass percentages from the EDS as a reference, the molar ratios of MgO to Al_2O_3 were calculated (Table III). The values contained within the brackets indicate by how much the measured amount was above (+) or below (-) the theoretical value for stoichiometric spinel.

Figure 5 shows the densification curve for the sintering cycle. The piston speed during the sintering cycle has been plotted with the temperature and pressure versus time. The total linear shrinkage for the powders with the LiF was 54.75 ± 1.50%, while for the powders without LiF it was 57.04 ± 1.28%. The powders sintered with LiF had a sudden onset of densification within the first hour and a half, and for the powders without LiF, there was a sudden onset of densification in the second hour and a half. The majority of the sintering occurred within the first three hours of the sintering cycle.

Figure 6 shows the densification curve for the first hour and a half. The applied pressure was a constant 10 MPa during this time. Initially both powders (with and without 1 wt.% LiF) underwent densification as the temperature increased from

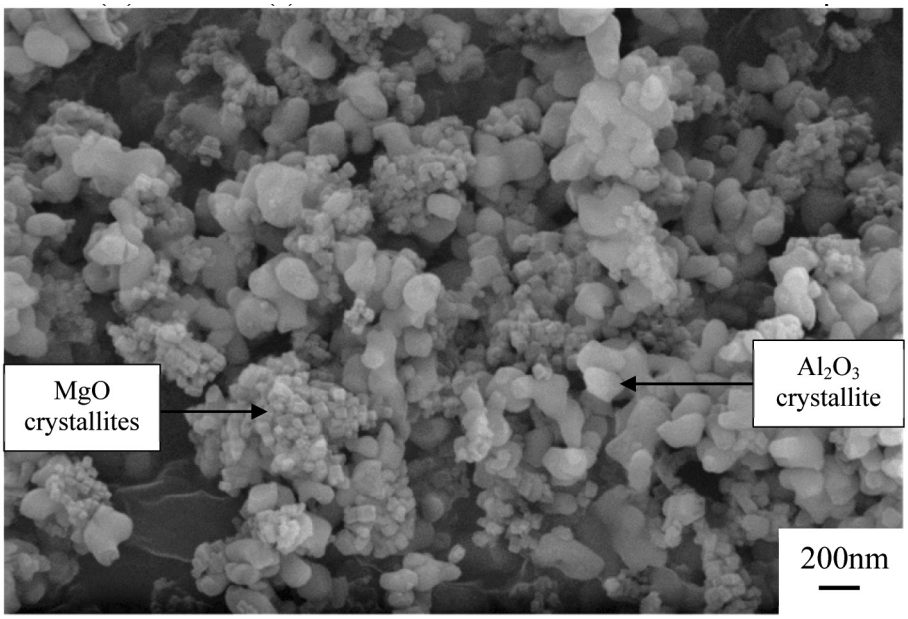

Figure 2: FEG-SEM image of the mixed Al_2O_3 – MgO powder

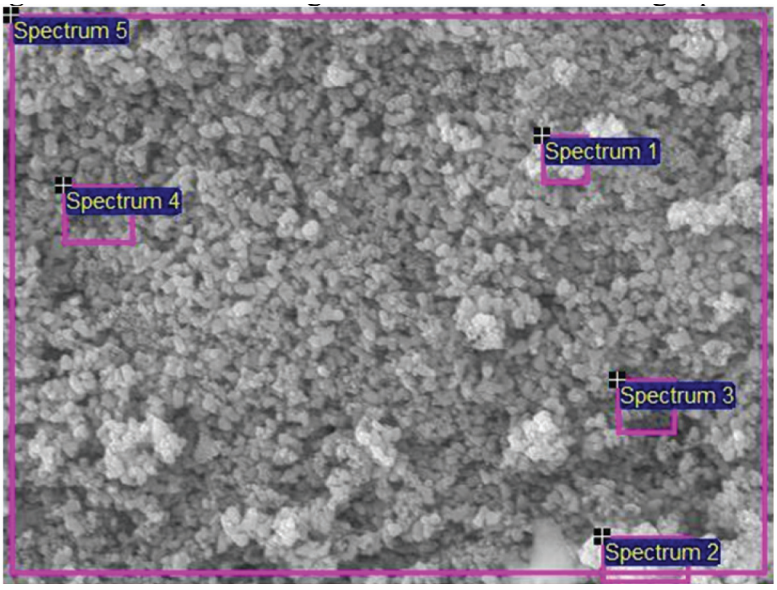

Figure 3: Area of analysis for the EDS measurements

Table III: Measured atomic mass percentages from the EDS analysis

	Spectrum				
Element	**1**	**2**	**3**	**4**	**5**
O	48.62 (+3.64)	50.46 (+5.48)	44.75 (-0.23)	40.37 (-4.61)	45.48 (+0.50)
Mg	15.61 (-1.48)	17.67 (+0.58)	21.30 (+4.21)	18.75 (+1.66)	17.09 (+0.00)
Al	35.77 (-2.16)	31.87 (-6.06)	33.95 (-3.98)	40.87 (+2.94)	37.43 (-0.50)
Al_2O_3/MgO	1.03 (+0.03)	0.81 (-0.19)	0.72 (-0.28)	0.98 (-0.02)	0.99 (-0.01)

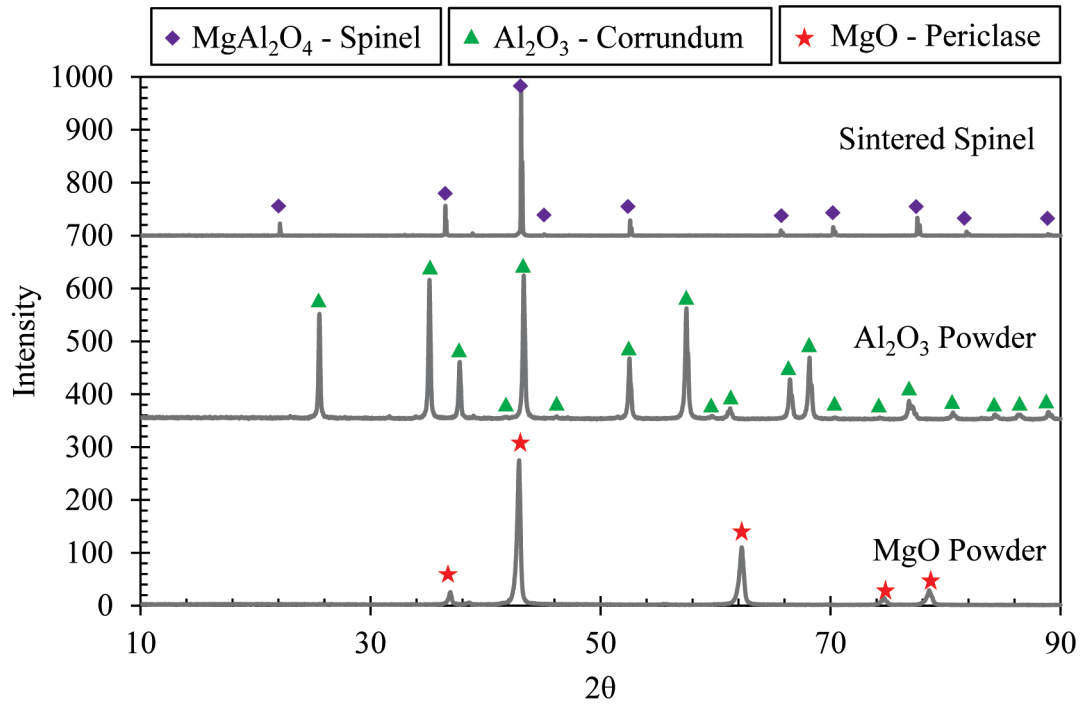

Figure 4: XRD spectra of the individual powders and a cross-sectioned processed spinel

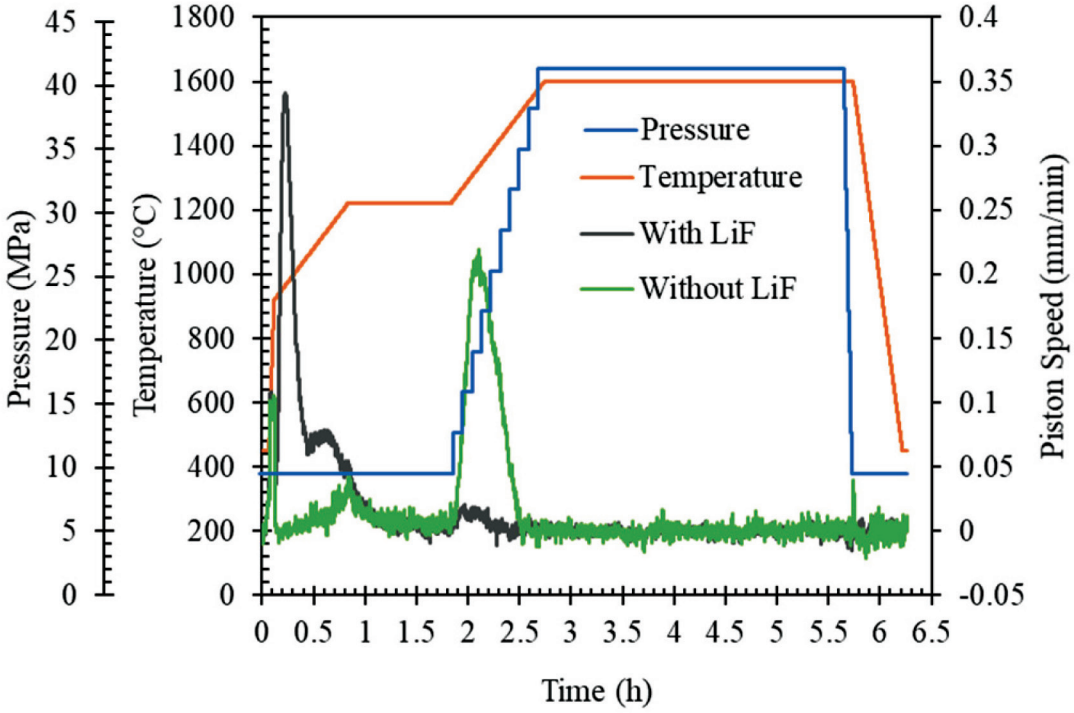

Figure 5: Piston movement during the sintering cycle with and without LiF additions

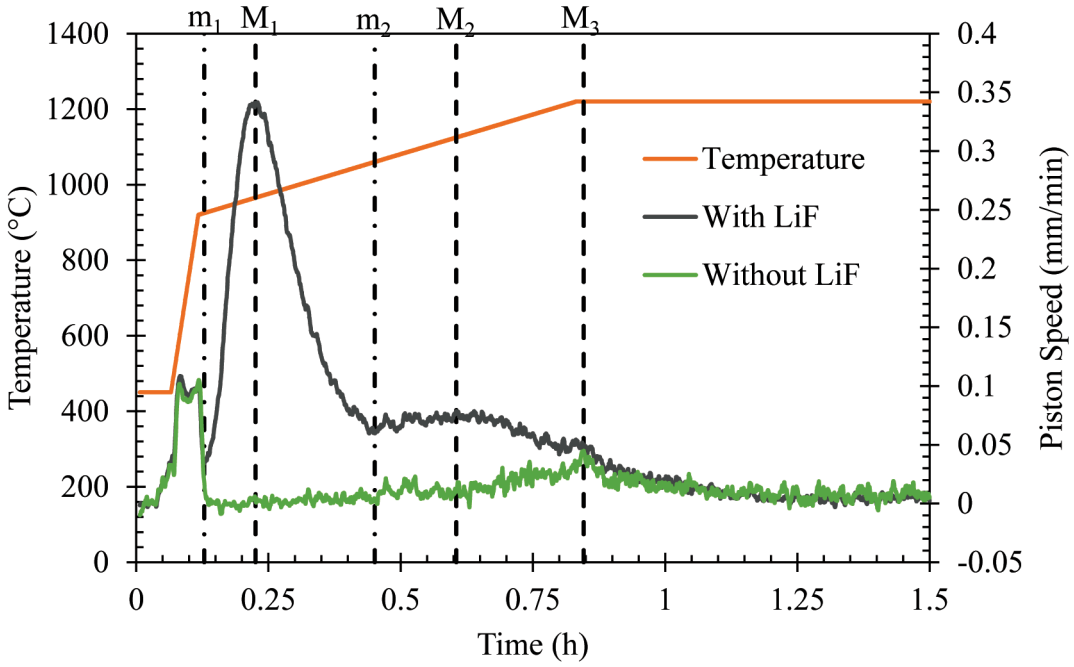

Figure 6: Densification curves for the first 1.5 hours

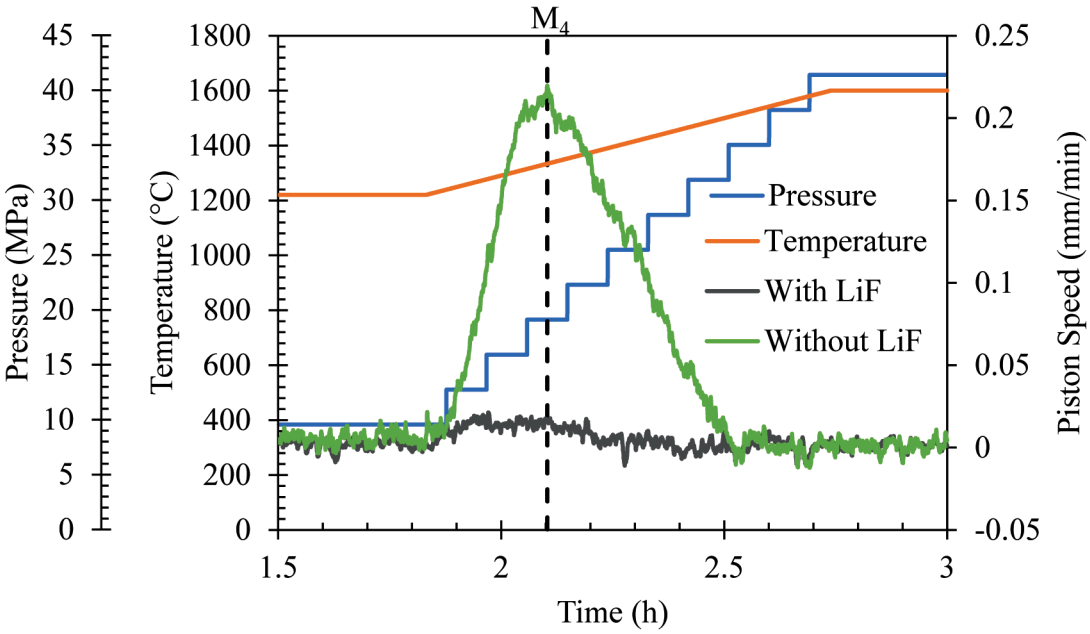

Figure 7: Densification curves from 1.5 to 3 hours

room temperature to 900°C. When the sample with LiF, reached ≈ 925°C (m_1) the piston speed began to increase until it reached a peak at ≈ 965°C (M_1). After this, the piston speed went through a local minimum at ≈ 1060°C (m_2) which was followed by a local maximum at ≈ 1125°C (M_2). The sample without LiF had a minor peak as the temperature reached 1220°C (M_3).

In Figure 7 the sintering curve is shown for the second hour and a half. During this time, the sample with LiF did not show any significant densification. The sample without the LiF however, peaked when the temperature and pressure reached 1333°C and 20MPa respectively (M_4).

The XRD spectra for the sintered sample containing LiF is shown in Figure 4. Only peaks associated with $MgAl_2O_4$ were present, no peaks associated with either Al_2O_3 or MgO were detected. An EDS scan was conducted over a fracture surface which is shown in Figure 8 along with the measured mass percentages in Table IV. The theoretical values for $MgAl_2O_4$ spinel are given in brackets.

Table IV: Measured atomic mass percentages from the EDS analysis of the fracture surface

Element	Weight %	Atomic %
O	45.66 (44.98)	57.85 (57.14)
Mg	16.07 (17.09)	13.40 (14.29)
Al	38.28 (37.93)	28.76 (28.57)

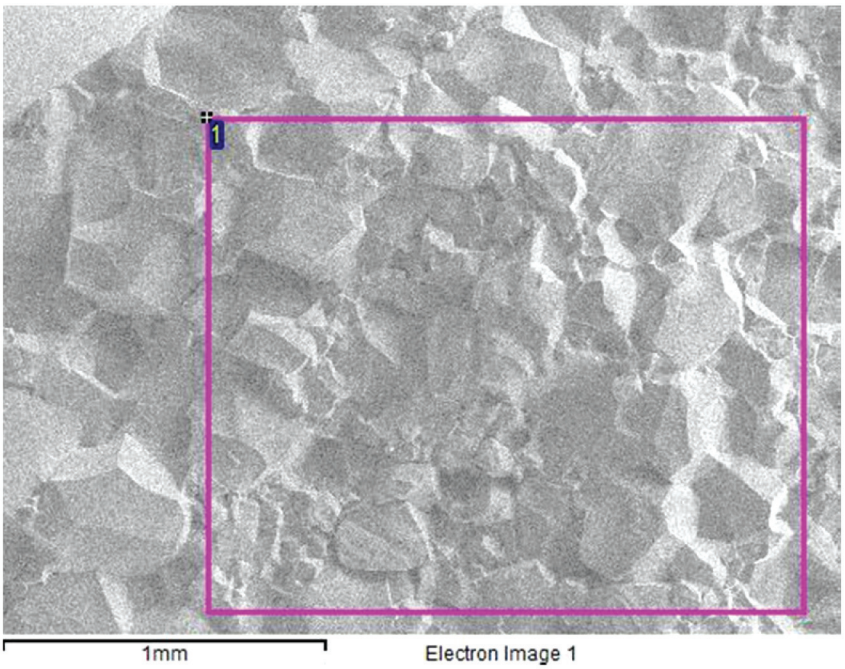

Figure 8: Area of analysis for the EDS measurement

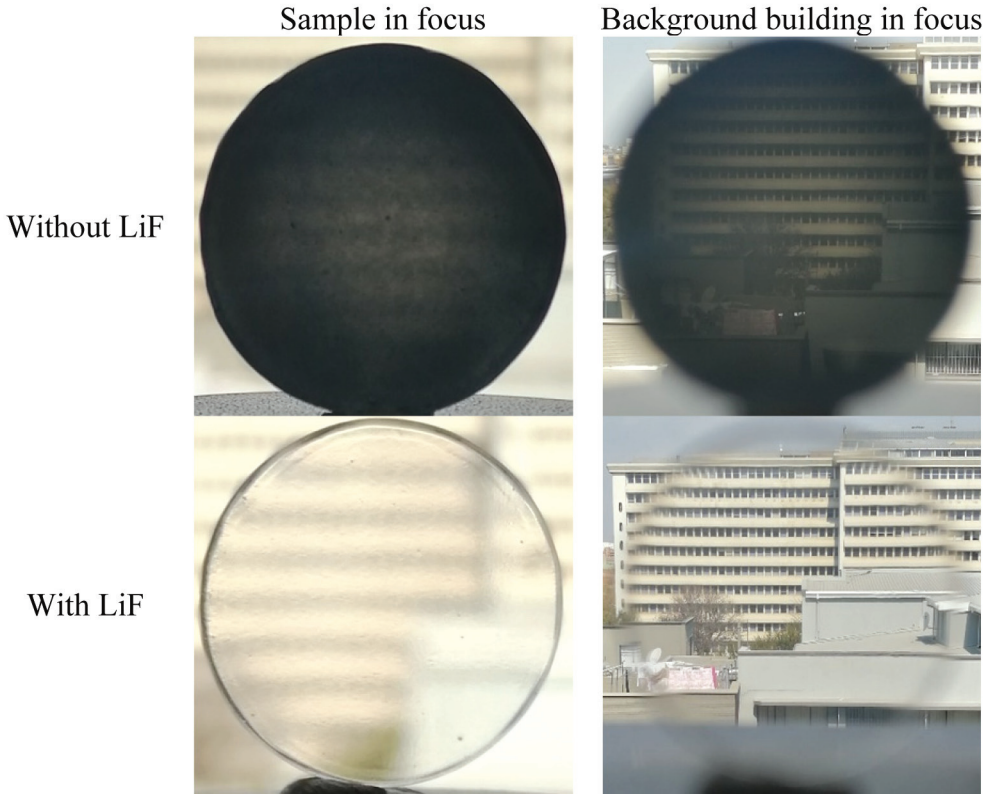

Figure 9: Images of the samples sintered, with and without LiF

The measured amount of aluminium was relatively higher than stoichiometric spinel. Thus, it was aluminium rich spinel that formed, whereas for the powder, the aluminium was slightly less, Spectrum 5 of Figure 3 and Table 3. This indicated that a portion of the Mg escaped during the sintering cycle. Figure 9 shows images of the sintered $MgAl_2O_4$ fabricated with and without LiF. The average transmittance of the samples sintered with LiF is shown in Figures 10 and 11. The blue shaded area is one standard deviation above and below this average. Other single stage sintering profiles from literature are also shown. Table V gives the measured transmittance at the wavelengths which correspond to the limits of the visible spectrum and the midpoint. Included in the table is the ratio between the measured transmittance and the theoretical maximum transmittance.

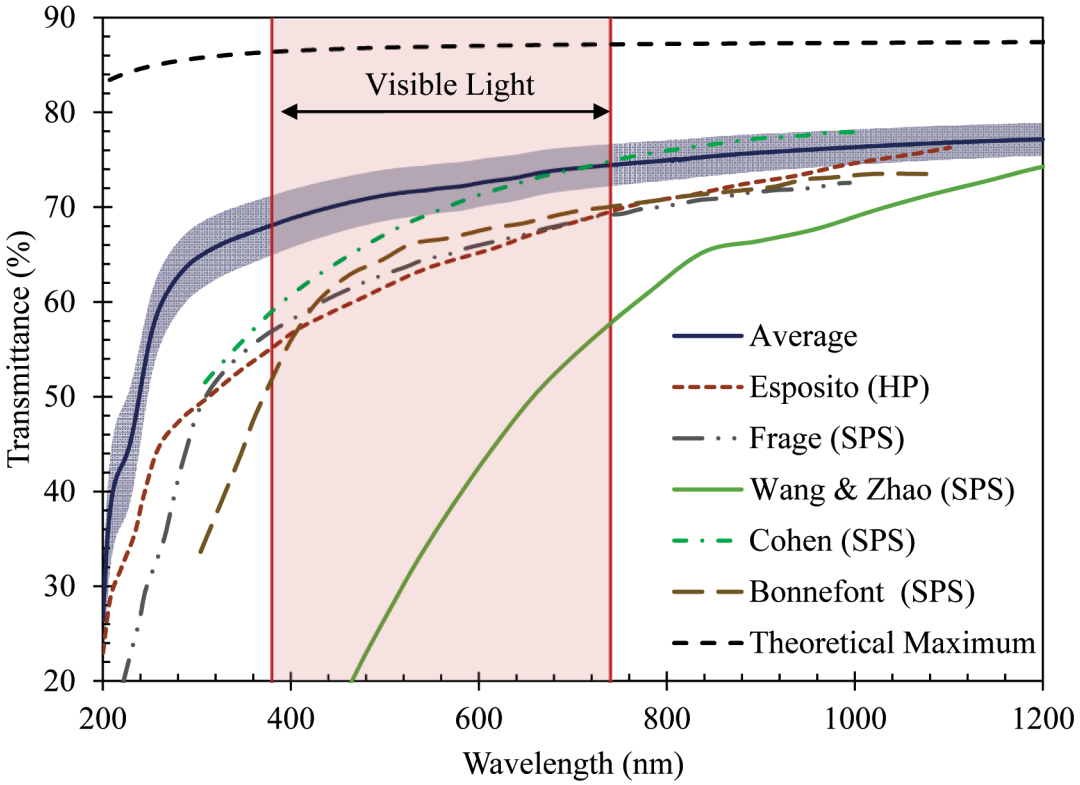

Figure 10: Transmittance spectra of the sintered spinel compared to those from (Esposito, et al., 2013) (Esposito (HP)), (Frage, et al., 2007) (Frage (SPS)), (Bonnefont, et al., 2012) (Bonnefont (SPS)), (Wang & Zhao, 2009) (Wang & Zhao (SPS)), (Cohen, et al., 2018) (Cohen (SPS)). The spectra were all normalised to a sample thickness of 3 mm

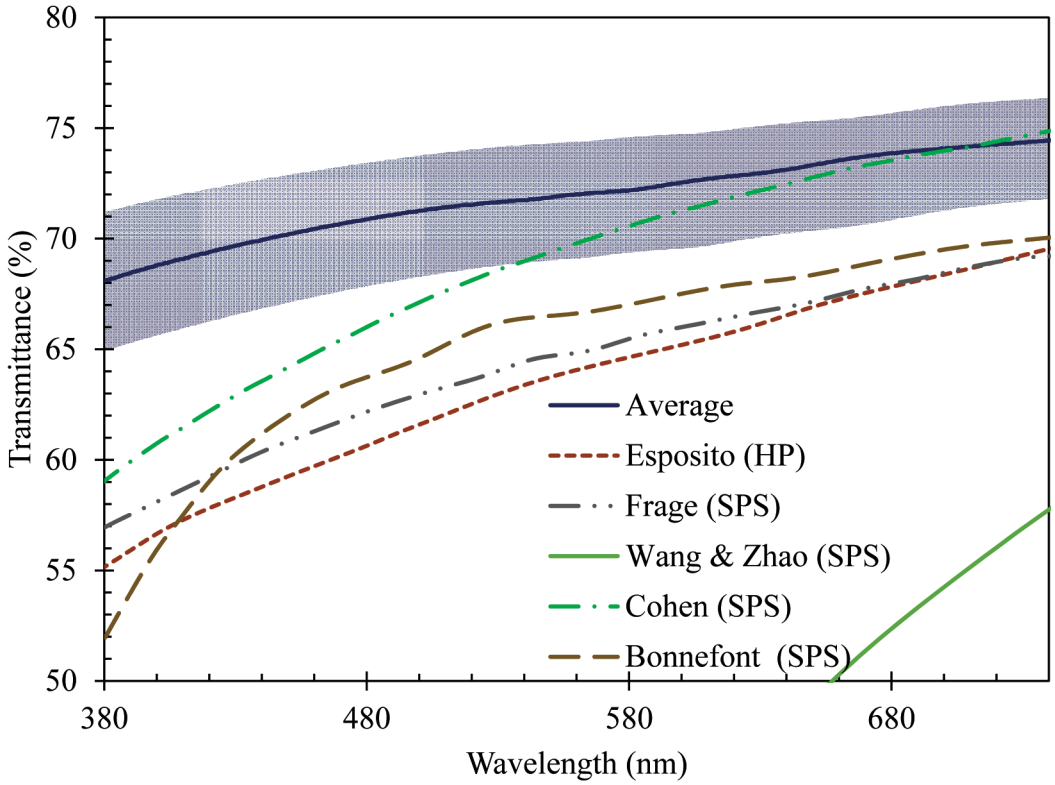

Figure 11: Transmittance spectra of the sintered spinel over the visible spectrum compared to those from (Esposito, et al., 2013) (Frage, et al., 2007) (Bonnefont, et al., 2012) (Wang & Zhao, 2009) (Cohen, et al., 2018). The spectra were all normalised to a sample thickness of 3 mm

Table V: The transmittance at the limits and mid-point of the visible spectrum

Wavelength (nm)	One stdev. Below (%)	One stdev. Above (%)	Average (%)	Range (%)	Tave/Tth
380	64.97	71.24	68.11	6.27	78.79
560	69.41	74.61	72.01	5.20	82.81
740	72.22	76.66	74.44	4.44	85.39

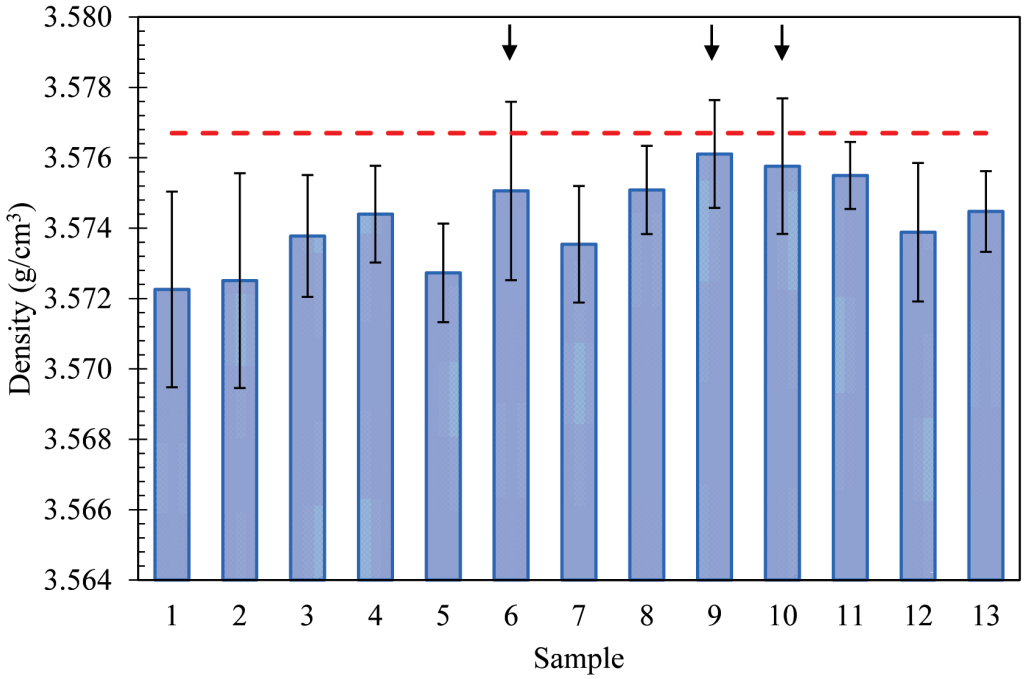

Figure 12: Densities of the sintered samples

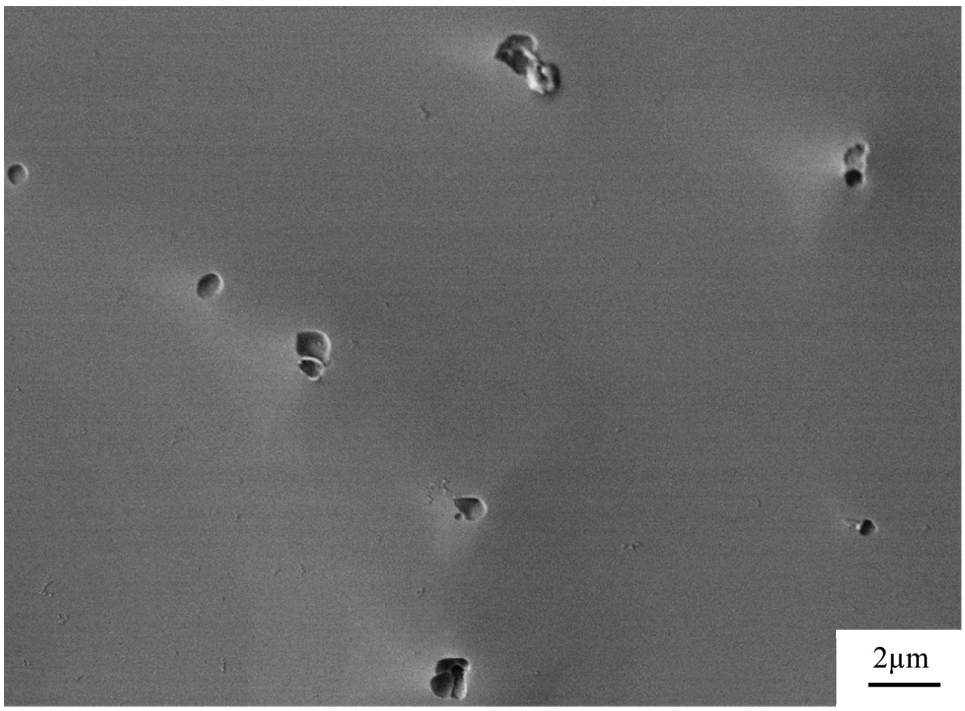

Figure 13: SEM micrograph of numerous pores on the surface of a grain

The densities of the samples are given in Figure 12. While the measured values were all close to the theoretical value of spinel, 3.5762 g/cm^3 (Navrotsky, et al., 1986) (Harris & Turri, 2013), they were all slightly less. Only three of the thirteen samples had uncertainties that went beyond the theoretical value. Thus, residual porosity should exist. This was confirmed by the SEM when analysing a fracture surface (Figures 13 and 14).

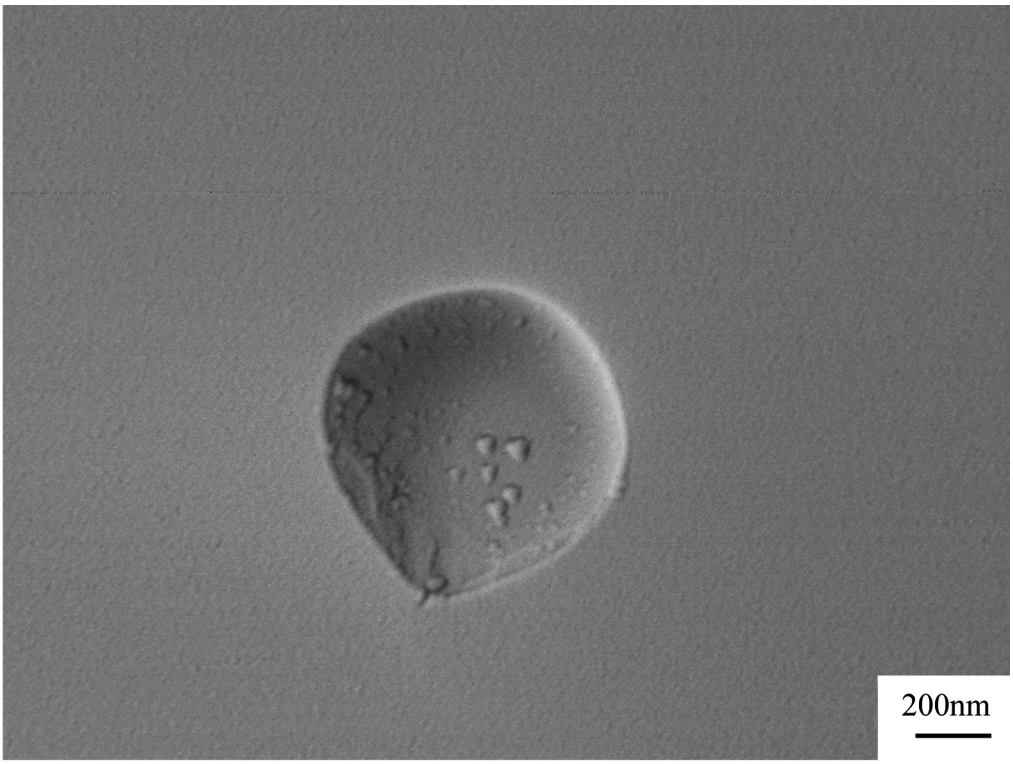

Figure 14: High magnification SEM micrograph of a pore

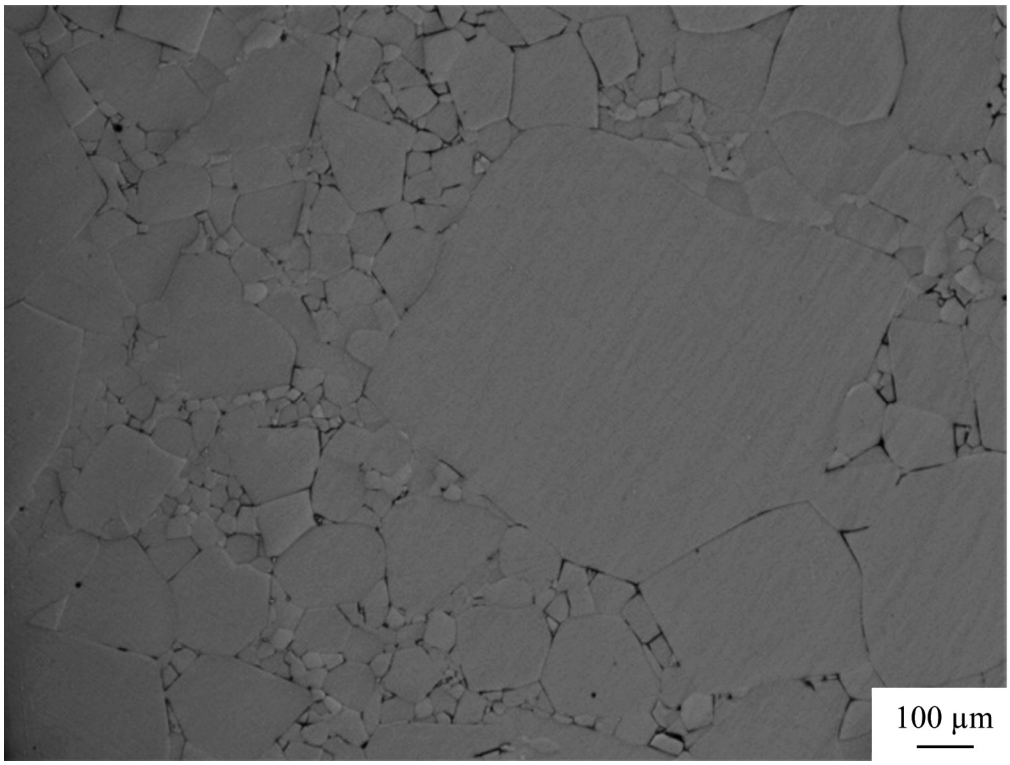

Figure 15: Optical microscope image of the etched surface of a $MgAl_2O_4$ sample

An image taken from the optical microscope of the etched surface is shown in Figure 15.

The linear intercept method was used to calculate the average grain size using multiple micrographs. The average grain-size using this method was measured to be 96 µm ± 34 µm. Furthermore, a frequency distribution was also determined. This was calculated by taking the average diameter of ≈750 grains (Figure 16). When the natural-logarithm of the natural-logarithm of the grain size (was plotted in a frequency distribution it formed a normal distribution, the insert of Figure 16. The arithmetic mean for the diameter calculated from the frequency

data was 45 µm ± 45 µm, whereas the geometric mean was 32.25 µm. The geometric mean of the fitted curve was 31.52 µm, labelled PDF in the insert of Figure 16. These values seem to greatly underestimate the size of the grains shown in Figure 15.

The "Area Percentage" distribution for this microstructure was estimated by assuming a cubic microstructure (for each grain, its largest and smallest diameter were multiplied to approximate its area) and this is shown in Figure 17.

This distribution in Figure 17 is bimodal. The small grains which individually contribute little to the total area, are numerous, thus form a peak in the distribution. The larger grains, which are far less numerous are, however so large that even a small number of them contribute a significant amount to the area. Approximately 67% of the grains (the grains < 50 µm) contribute only ≈12.5% of the area. The "Area Percent" distribution seemed to better describe the micrograph in Figure 15. The weighted area diameter was 236 µm and the weighted standard deviation was 208 µm. This value is much higher than the other two methods. However, this method accounts for the fact that even a small number of large grains can account for a large portion of the micrograph.

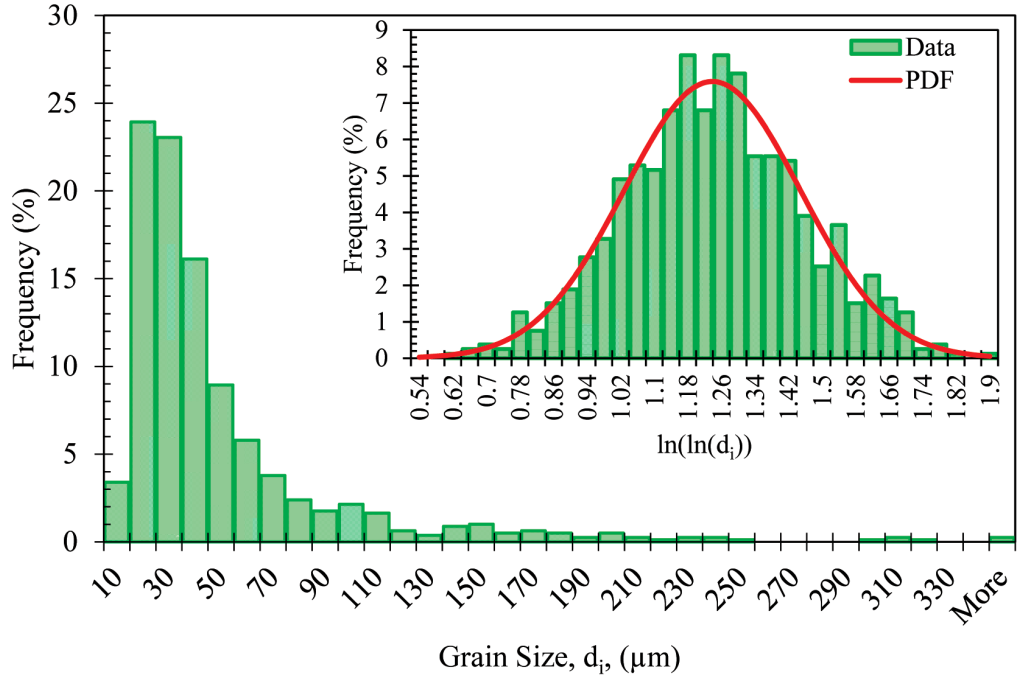

Figure 16: Normal distribution obtained by taking the natural logarithm of the natural logarithm of the grain size

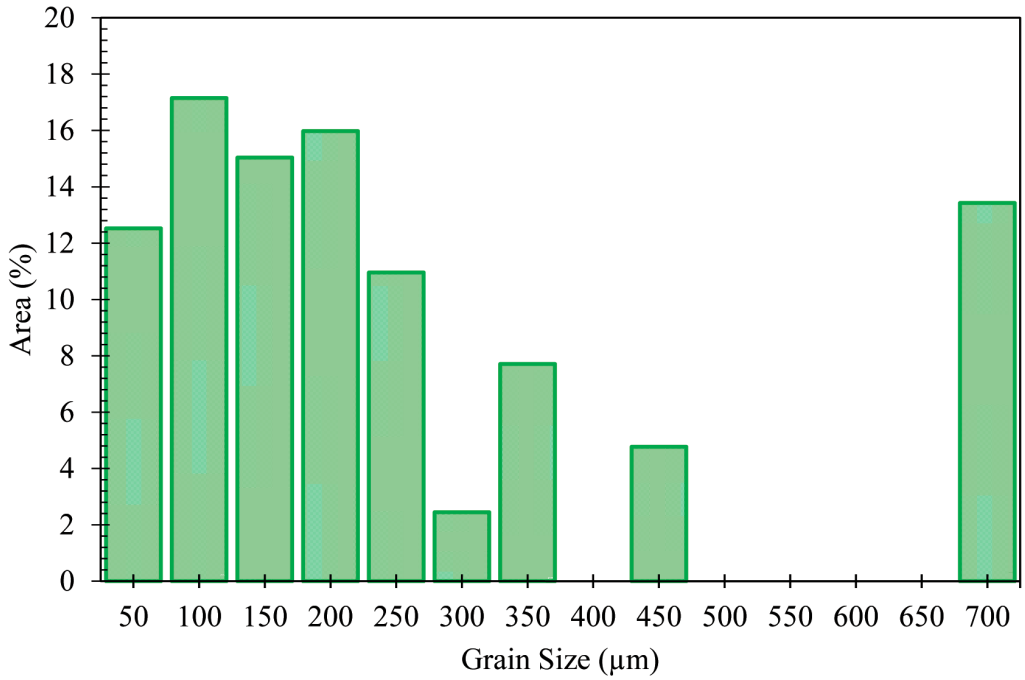

Figure 17: "Area Percent" distribution of the measured grains

Mechanical properties

The average fracture toughness was measured to be 1.56 $MPa.m^{-1/2}$ ± 0.26 $MPa.m^{-1/2}$ and the average hardness was 1245 Hv ± 36 Hv. The nominal strength was 145 MPa and the Weibull Modulus was 3.91. For comparison, Rothman, et al. (2014) measured a strength of 150 ± 20 MPa for a spinel sample with a grain size of 40 µm.

Regrettably, the measurement for the fracture toughness was dubious. Figure 18 shows a characteristic indent from which the hardness and fracture toughness values were determined. Alongside the image is what an ideal indent on spinel looks like. There are many cracks surrounding the indent on the transparent sample and they do not all originate from a corner of the indent. Spalling was also observed. Because there were many cracks, determining which cracks should be measured was difficult. This would likely prevent the attainment of consistent measurements.

However, the diagonals of the indents were easily measured, thus the hardness values were more reliable. Table 6 shows the measured hardness values of this work and of other authors. The hardness of these samples was slightly less than the reported values.

Table VI: Measured hardness of this work and of other authors, (Esposito, et al., 2013) (Frage, et al., 2007) (Rothman, et al., 2014).

Author	Hardness (Hv)
Rothman, et al. (2014)	1600 ± 28
Rothman, et al. (2014)	1450
Esposito, et al. (2013)	1420 ± 60
Esposito, et al. (2013)	1390 ± 60
Frage, et al. (2007)	1300 ± 50
This work	1245 ± 36

The samples fractured with the B3B test showed a qualitative relationship between the number of pieces the samples fractured into and the force required to cause the fracture, Figure 19.

The fracture surface of a sample is shown in Figure 20. There was a mix of transgranular and intergranular fracture surfaces.

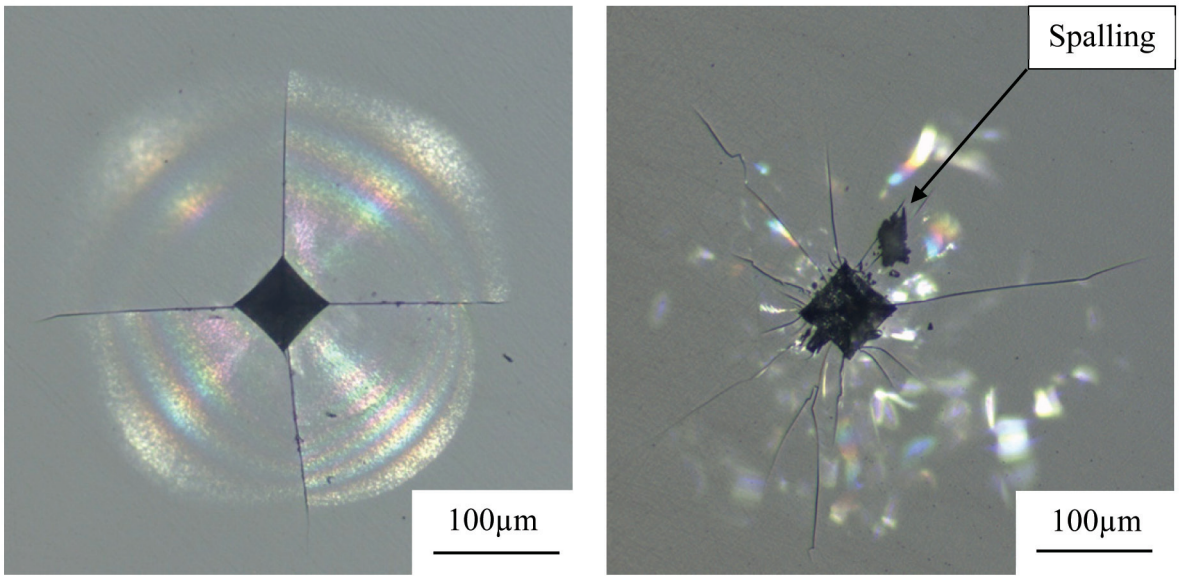

Preferable indent on a spinel sample (grain size ~270 nm)

Indent on the transparent sample (grain size ~236 µm)

Figure 18: Hardness indent on the transparent sample as well as on a spinel sample with a much smaller grain size

87MPa 126MPa 184MPa

Figure 19: Samples fractured by the B3B test. The diameter of the disks was 20 mm

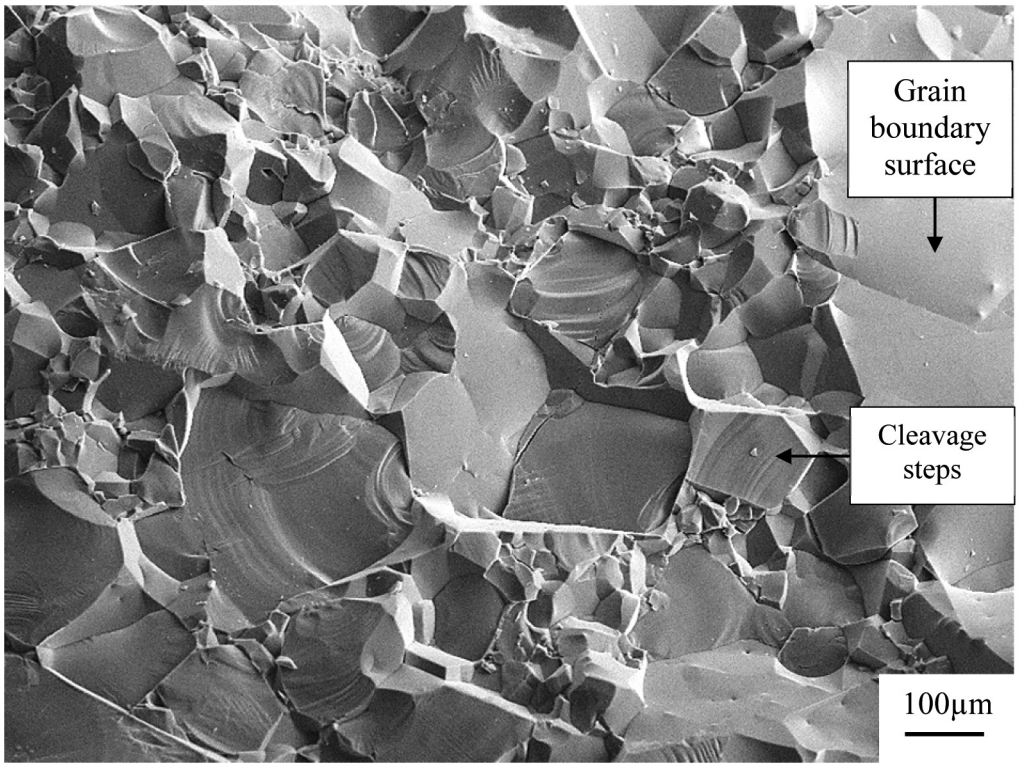

Figure 20: Low magnification SEM micrograph of the spinel's fracture surface

Discussion

Powder analysis

The particle size analyser measured values similar to those of the suppliers; however, these values seem to be greatly exaggerated when looking at the SEM micrograph shown in Figure 2. As the milling was relatively gentle, only 110 rpm, it was unlikely that the powders were milled from the sizes measured by the PSA to the sizes shown in Figure 2. The powders were initially composed of soft agglomerates. These tend to form in powders with small crystallite sizes that are kept in a dry state (Staiger, et al., 2002). The milling broke apart these agglomerates allowing the powder to mix on a much smaller scale.

The SEM image of the mixed powders, Figure 2, shows that the powders did not separate to individual crystallites, rather there were still aggregates. Also, the EDS spectra shows that there were alumina rich and magnesia rich areas within the powder, Figure 3 and Table 3, further evidence of aggregation.

The EDS spectra over the entire area shown in Figure 3 indicates that the powder was slightly MgO rich, the ratio of Al_2O_3 to MgO, n, was 0.9865 instead of 1. However, according to the phase diagram given by (Hallstedt, 1992), at 1600°C (which was the sintering temperature), the spinel structure can accommodate a range of $0.92<n<1.99$. Therefore, all the MgO and Al_2O_3 were expected to react to form $MgAl_2O_4$. This was confirmed by the XRD spectra of the sintered ceramic, Figure 4, which did not contain any peaks associated with either starting powder.

Sintering data

The addition of LiF lowered the required temperature for appreciable densification from 1333°C (M_4) to 965°C (M_1) and the pressure from 20 MPa to 10 MPa (Figure 5). This observation coincides with the literature as LiF has been observed to reduce the temperature of the spinel formation reaction, (Huang & Sun, 1997), (Rozenburg, et al., 2007), (Meir, et al., 2008), (Esposito, et al., 2013), and reduce the temperature at which spinel acquires full density, (Reimanis & Kleebe, 2007) (Rozenburg, et al., 2008), , (Meir, et al., 2008), (Esposito, et al., 2015).

For the powder with the LiF, the temperature at which the first peak (M_1 in Figure 6) occurred was in agreement to the work done by Frage et al. (2007). When Frage et al. (2007) analysed the relative piston travel, they found that densification started at ~950°C. The temperature at which densification began determined by both this work and Frage et al. (2007) was slightly higher than that of Meir et al. (2008), who detected a sudden increase in the densification of the samples containing LiF at ~870°C. Meir et al. (2008) deduced that the cause of the peak was due to the melting of the LiF.

The temperature of the first peak (~965°C) was appreciably higher than the melting temperature of LiF (848°C), therefore the reason given by Meir et al. (2008) for the densification peak in their work was unlikely to be the case in this work. Rather, this work's results support the mechanism that Esposito et al. (2013) adapted from Rozenburg et al. (2007). The onset of the reaction between the LiF, MgO, and Al_2O_3 is expected to begin between 900°–1000°C and can be written as Equation 1 (Esposito, et al. (2013).

$$3LiF_{(l)} + MgO_{(s)} + Al_2O_{3(s)} \longrightarrow LiF{:}MgF_{2(l)} + 2LiAlO_{2(s)} \quad \text{Equation (1)}$$

Thus, the addition of the LiF resulted in a liquid phase at the temperature of the first peak, either liquid LiF (as suggested by Meir et al. (2008)) but more likely in this case the LiF:MgF_2 (as suggested by Esposito et al. (2013)). The liquid phase would have enhanced the densification rate through liquid phase sintering. The liquid phase penetrated the powdered compact and promoted the spinel formation reaction by mass transport which would have been more rapid than the solid-state diffusion. The increase in the rate of densification was manifested in the width of the densification peaks as well. The duration of the densification peak for the LiF-containing sample was 0.32 hours (Figure 6), whereas the samples without the LiF had a duration of 0.63 hours (Figure 7), nearly twice as long.

Besides the formation of a liquid phase, the formation of the $LiAlO_2$ was also expected to have occurred according to Equation 1. The $LiAlO_2$ would have assisted densification by the formation of oxygen vacancies (Rozenburg, et al., 2007). Rozenburg et al. (2008) concluded that the rate-determining mechanism in spinel densification was oxygen lattice diffusion, which was also stated by Aksel (2004). The generation of the oxygen vacancies by the $LiAlO_2$ formation lowers the energy required for oxygen lattice diffusion, thereby enhancing spinel densification at lower temperatures (Rozenburg, et al., 2008). The cumulative effect of the discussed phenomena was a reduction in the activation energy for sintering spinel, which resulted in the lower temperature and pressure required for densification to begin.

The second peak (M_2 in Figure 7) coincided with the vaporisation of the liquid LiF and MgF_2 phases (LiF:MgF_2 in Equation 1) at 1050°C (Rozenburg, et al., 2007). This was further evidence that supported the occurrence of the reaction shown in Equation 1.

Sintered sample analysis

The EDS spectra over the fracture surface shows that the relative amount of Mg was less than stoichiometric $MgAl_2O_4$. As the powder was Al rich, Mg must have escaped during the sintering cycle. This would be possible as MgF_2 was expected to have vapourised after the temperature surpassed 1050°C. This would have enabled a portion of the Mg to leave the system as a gaseous species. However, the XRD spectra shows that the resulting phase was still $MgAl_2O_4$ spinel. This was possible as the spinel structure can accommodate a range of ratios between the MgO and Al_2O_3 (Hallstedt, 1992).

The samples sintered in the presence of the LiF were transparent (Figure 9). Their transmission was higher than other values reported in literature for single-stage sintering processes, Figure 10, especially within the visible spectrum, Figure 11. Without the LiF the samples showed excessive darkening, likely caused by carbon contamination originating from the graphitic tooling used within the SPS furnace. The extent of carbon contamination was likely exacerbated due to the long sintering cycle.

Table 5 shows that the transmission spectrum was still below the theoretical value by an appreciable amount, and that the measured and relative transmittance decreased as the wavelength decreased. All the sintered samples had densities slightly lower than the theoretical value, even when including the uncertainty in the measurements. Thus, porosity contributed to the reduction in transmittance.

Pores were observed when the fracture surface was analysed with the FEG-SEM (Figures 13 and 14). The pores were present at grain-boundaries and were hemispherical. Pores were not observed at triple points. Thus, the residual porosity needs not be a result of insufficient densification but rather the entrapment of gas. The rounded shape appears to be from the exertion of isostatic pressure that would develop when entrapped gas was heated. The addition of LiF resulted in the formation of a liquid phase. As the liquid phase began to form, it would likely surround the Al_2O_3, MgO and $MgAl_2O_4$ particles. Liquid LiF has been found to have a low wetting angle with spinel (Meir, et al., 2008). This would result in a process-driving capillary pressure at the contact points between particles. This capillary pressure would force the particles closer together, thus increasing shrinkage and lowering porosity, while also changing the pore size and shape (Amor´os, et al., 2007). As the porosity decreases, pores would begin to close. These closed pores could trap the liquid phase. As the temperature continued to increase, this liquid phase would vaporise and form a gas. The trapped gas would exert a pressure on the pore walls. If the temperature was increased further, the pressure of the gas would exceed the capillary pressure and the pores would begin to grow, thus the porosity would start to increase (Amor´os, et al., 2007). Therefore, simply increasing the sintering temperature may not necessarily reduce the porosity.

The porosity could potentially be reduced through better powder preparation. The powders used had very small crystallites; however, the presence of agglomerates and

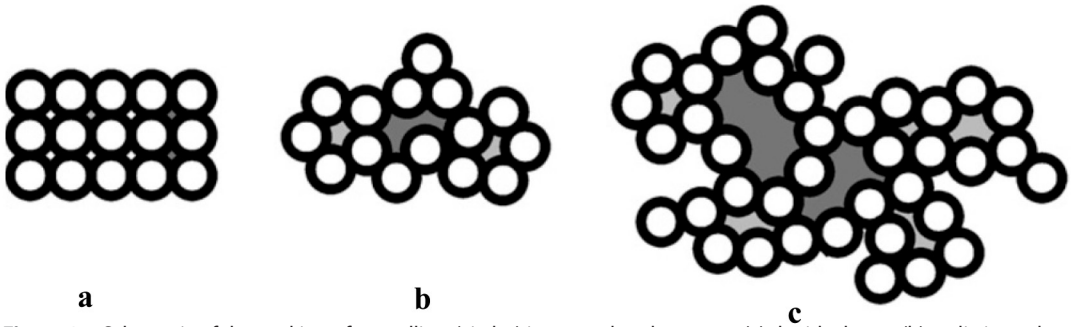

Figure 21: Schematic of the packing of crystallites (circles) in a powdered compact (a) the ideal case, (b) realistic goal and (c) poorly process powder (Goldstein, 2012)

aggregate was confirmed. Depending on the relative orientation of these aggregates, the attainment of full density may not be possible. Due to the presence of the aggregates, the ideal ordered arrangement for the particles, depicted in Figure 21.a, was unattainable. However, the arrangement shown in Figure 21.b. would be a realistic goal. The arrangement shown in Figure 21.c. would preclude the attainment of a fully sintered ceramic (Goldstein, 2012).

The agglomerates were expected to break up during the milling process, and not be present during the sintering process. However, after milling the slurry was dried using a rotary evaporator. This drying process could result in partial re-agglomeration. Therefore, even though these powders did have exceedingly small crystallites (< 50 nm), the small crystallite size was likely underutilised, as the particle size would be represented by the aggregate size.

The presence of these aggregates would mean that the packing arrangement of the powders could be the arrangement shown in Figure 21.b or 21.c, depending on the relative orientation of the irregularly shaped aggregates. The poor packing would allow for the entrapment of gas within the sintered ceramic, leading to the generation of the hemispherical pores.

This would have resulted in a random chance of a sample being well packed or poorly packed. This could be the reason for the low Weibull modulus and the fairly wide range of transmittance.

Grain structure

The grain structure showed an extremely wide range of grain sizes, the smallest measured grain size was ≈6 µm, while the largest was ≈700 µm. The grain sizes were also much larger than the sizes of the initial powders, particularly since grains grow from crystallites, not aggregates. Extensive grain growth was expected due to the long sintering time of three hours at 1600°C. The grain size distribution was normally distributed when the natural logarithm of the natural logarithm of the grain size was plotted as a frequency distribution. The Shapiro-Wilk's test was used to test the distribution shown in the insert of Figure 16 for normalcy. There was not statistically significant evidence to reject the hypothesis that the data was taken from a normal distribution.

Due to the wide grain size most grains contributed negligibly to the area distribution of the microstructure (as area is proportional to d^2). Thus, the area distribution formed a bi-modal distribution. The small grains which individually contribute little to the total area, are numerous, thus form a peak in the distribution. The larger grains, which are far less numerous are, however, so large that even a small number of them contribute a significant amount to the area. This resulted in a microstructure which was essentially heterogeneous.

A distribution of this kind made it difficult to determine a suitable value for what could be considered a representative grain size of these samples. Depending on the method used, there was a substantial difference in grain size. As 'grain size' is such an important metric when comparing the mechanical properties of materials, a suitable value needs to be determined.

The calculated average grain size from the distribution was less than half the value measured by the linear intercept method. The measurement from both the distribution and the linear intercept method seem far smaller than what the micrograph in Figure 15 shows. Therefore, neither the linear intercept method nor measuring the average size of each grain produced a satisfactory value for the mean grain size. These methods could not accurately represent the grain-size of the heterogeneous microstructure. This occurred because the small grains, which contributed little to the area of the micrograph were weighted equally to the large grains in the determination of the average grain size. As the small grains were more numerous than the larger grains (Figure 16), the average was skewed towards the smaller grain size.

The weighted area diameter, 236 µm ± 208 µm, looks as though it has no practical use as the average value (236 µm) is similar to the standard deviation (208 µm), thus it would seem that the uncertainty in the measurement was as large as the actual measurement. However, this was not the case. The standard deviation was relatively high because the grain size varied over such a wide range. Thus, the standard deviation of 208 µm does not imply that the uncertainty in the measurement was relatively high, just that the distribution of the grain sizes was wide. This accurately describes the microstructure depicted in the micrograph of Figure 15.

The heterogeneous microstructure of $MgAl_2O_4$ sintered in the presence of LiF has also been observed by Reimanis & Kleebe (2007), Rozenburg et al. (2008), and Rothman et al. (2014). The Li^+ cations are expected to be incorporated into the spinel matrix formed oxygen vacancies, Equation 2.

$$3Li \xrightarrow{Spinel} 2Li'_{Mg} + Li''_{Al} + 2V''_{O} \qquad \text{Equation (2)}$$

This lowered the energy for oxygen lattice diffusion, which enhanced the spinel grain growth (Rozenburg, et al., 2007). The spinel grains which incorporated the Li^+ cations grew at a faster rate than those grains which did not.

Mechanical properties

Besides making it difficult to quantify a representative grainsize value, the heterogenous microstructure also made it difficult to get a consistent value for hardness and fracture toughness. The reason for this was because the hardness indent could occur over a single large grain, or over many small grains. As the local grain size varied randomly over the surface of the ceramic, the hardness and fracture toughness measurement would vary in accordance with the local grain size.

Overall, the mechanical properties of these samples were below par. The hardness was less than the reported values of other authors and spread of biaxial flexural strength was significant. While the indentation fracture toughness was measured, the test was unreliable as the area around the indent had numerous cracks and spalling occurred. Such local disruptions are likely to

affect the measured value of the fracture toughness (Anstis, et al., 1980). The disruptions occurred due to the large grain size of the transparent samples (Figure 18). Anstis et al. (1980) determined that if the grain size is of the same order as the crack-length, then the indentation will likely result in excessive damage around the indent. This was the case for the transparent samples. Figure 18 also shows the indent of a spinel sample with a much smaller grain size, which resulted in a much better indent, however, this sample was not transparent as the sintering time was very short to ensure the grain size remained small. Thus, the value of the fracture toughness would need to be verified by an alternative method to indentation fracture such as the single edge notched beam method (Wang & Atkinson, 2015).

The Weibull modulus of the samples was 3.91. This was low as the value of the Weibull modulus for many structural ceramics is around 10 (Petrovic, 1987). This indicates that the spread of the fracture stress for these samples was unusually high. Ceramic materials are sensitive to the largest flaw size present. If there was a wide spread of strength, it would imply that the process used to fabricate these ceramics resulted in a wide spread of flaw sizes, not necessarily within a single sample, but between samples.

The pores that were present could have varied in size depending on the initial powder compact and the degree of pore coalescence. Depending on how the aggregates within the powders were packed, either Figure 21.b or 21.c could occur. Also, depending on the amount of gas within a pore before it closes the pore could be large or small. These factors introduced an element of randomness to the size of the pores within the samples. This randomness would have contributed to a spread in biaxial-fracture strength.

Conclusions

The fabrication of a transparent spinel disk using an SPS furnace and the sintering aid LiF in a single stage sintering process did achieve a transmission of visible light of ≈70%. The residual porosity contributed to the decrease in transmission. The cause of the porosity is likely the generation of a gas during sintering as well as non-ideal packing of the powders. The addition of LiF and the long sintering times resulted in a heterogenous microstructure which could not easily be quantified. The mechanical properties of the spinel fabricated in this work were inferior to those given in the literature. However, the transmission was higher when compared to other single stage sintering processes. The large spread of fracture strengths would preclude this material's use as a material for transparent armour or window systems in space craft die to its stochastic failure probability.

Dates

Received: 01/09/2021
Accepted: 18/01/2022
Published: 30/03/2022

References

Aksel, C., 2004, Spinel formation, reaction conditions and densification properties of magnesia-spinel composites. *Key Engineering Materials* 264-268, 1071–1074. https://doi.org/10.4028/www.scientific.net/KEM.264-268.1071

Amor'os, J., Orts, M.J., García-Ten, J., et al., 2007, Effect of the green porous texture on porcelain tile properties. *Journal of the European Ceramic Society* 27, 2295–2301. https://doi.org/10.1016/j.jeurceramsoc.2006.07.005.

Anstis, G.R., Chantikul, P., Lawn, B.R., et al., 1980, A critical evaluation of indentation techniques for measuring fracture toughness: I, direct crack measurements. *Journal of the American Ceramic Society* 64(9), 533–538. https://doi.org/10.1111/j.1151-2916.1981.tb10320.x.

Benitez, T., Gómez, S.Y., De Oliviera, A.P.N., et al., 2017, Transparent ceramic and glass-ceramic materials for armor applications. *Ceramics International* 43(16), 13031–13046. https://doi.org/10.1016/j.ceramint.2017.07.205.

Bonnefont, G., Fantozzi, G., Trombert, S., et al., 2012, Fine-grained transparent MgAl2O4 spinel obtained by spark plasma sintering of commercially available nanopowders. *Ceramics International* 38(1), 131–140. https://doi.org/10.1016/j.ceramint.2011.06.045.

Cohen, S., Ratzker B., Sokol, M., et al., 2018, Polycrystalline transparent magnesium aluminate spinel processed by a combination of spark plasma sintering (SPS) and hot isostatic pressing (HIP). *Journal of the European Ceramic Society* 38(15), 5153–5159. https://doi.org/10.1016/j.jeurceramsoc.2018.07.024.

Esposito, L., Piancastelli, A., Martelli, S., 2013, Production and characterization of transparent MgAl2O4 prepared by hot pressing. *Journal of the European Ceramic Society* 33(4), 737–747. https://doi.org/10.1016/j.jeurceramsoc.2012.10.013.

Esposito, L., Piancastelli, A., Miceli, P., et al., 2015, A Thermodynamic approach to obtaining transparent spinel (MgAl2O4) by hot pressing. *Journal of the European Ceramic Society* 35(2), 651–661. https://doi.org/10.1016/j.jeurceramsoc.2014.09.005.

Frage, N., Cohen, S., Meir, S., et al., 2007, Spark plasma sintering (SPS) of transparent magnesium-aluminate spinel. *Journal of Materials Science* 42, 3273–3275. https://doi.org/10.1007/s10853-007-1672-0.

Gallo, L., Villas Boas, M.O.C., Rodrigues, A.C.M., et al., 2019, Transparent glass-ceramics for ballistic protection: Materials and challenges. *Journal of Materials Research and Technology* 8(3), 3357–3372. https://doi.org/10.1016/j.jmrt.2019.05.006.

Ganesh, I., 2013, A review on magnesium aluminate (MgAl2O4) spinel: Synthesis, processing and applications. *International Materials Reviews* 58(2), 63–112. https://doi.org/10.1179/1743280412Y.0000000001.

Goldstein, A., 2012, Correlation between MgAl2O4 spinel structure, processing factors and functional properties of transparent parts (Progress Review). *Journal of the European Ceramic Society* 32(11), 2869–2886. https://doi.org/10.1016/j.jeurceramsoc.2012.02.051

Hallstedt, B., 1992, Thermodynamic assessment of the system MgO-Al2O3. *Journal of the American Ceramic Society* 75(6), 1497–1507. https://doi.org/10.1111/j.1151-2916.1992.tb04216.x.

Harris, D., Turri, G., Seaver, R., et al., 2013, Optical and thermal properties of spinel with revised (increased) absorption at 4 to 5μm wavelengths and comparison with sapphire. *Optical Engineering* 52(8), 087113-1–087113-12. https://doi.org/10.1117/1.OE.52.8.087113.

Huang, J.-L., Sun, S.-Y., Ko, Y-C., 1997, Investigation of high-alumina spinel: Effect of LiF and CaCO3 addition. *Journal of the American Ceramic Society* 80(12), 3237–3241. https://doi.org/10.1111/j.1151-2916.1997.tb03259.x.

Krell, A., Hutzler, T., Klimke, J., 2009, Transmission physics and consequences for materials selection, manufacturing, and applications. *Journal of the European Ceramic Society* 29(2), 207–221. https://doi.org/10.1016/j.jeurceramsoc.2008.03.025.

Krell, A., Klimke, J., Hutzler, T., 2009, Transparent compact ceramics: Inherent physical issues. *Optical Materials* 31(8), 1144–1150. https://doi.org/10.1016/j.optmat.2008.12.009.

Meir, S., Kalabukhov, S., Froumin, N., et al., 2008, Synthesis and densification of transparent magnesium aluminate spinel by SPS processing. *Journal of the American Ceramic Society* 92(2), 358–364. https://doi.org/10.1111/j.1551-2916.2008.02893.x.

Navrotsky, A., Wechsler, B.A., Geisinger, K., et al., 1986, Thermochemistry of MgAl2O4-Al8/3O4 defect spinels. *Journal of the American Ceramic Society* 69(5), 418–422. https://doi.org/10.1111/j.1151-2916.1986.tb04772.x.

Petrovic, J.J., 1987, Weibull statistical fracture theory for the fracture of ceramics. *Metallurgical Transactions A* 18, 1829–1834. https://doi.org/10.1007/BF02647012.

Reimanis, I.E. & Kleebe, H-J., 2007, Reactions in the sintering of MgAl2O4 spinel doped with LiF. *International Journal of Materials Research* 98(12), 1273–1278. https://doi.org/10.3139/146.101591.

Rothman, A., Kalabukhov, S., Sverdlov, N., et al., 2014, The effect of grain size on the mechanical and optical properties of spark plasma sintering-processed magnesium aluminate spinel MgAl2O4. *International Journal of*

Applied Ceramic Technology 11(1), 146–153. https://doi.org/10.1111/j.1744-7402.2012.02849.x.

Rozenburg, K., Reimanis, I., Kleebe, H-J., et al., 2007, Chemical interaction between LiF and MgAl2O4 spinel during sintering. *Journal of the American Ceramic Society* 90(7), 2038–2042. https://doi.org/10.1111/j.1551-2916.2007.01723.x.

Rozenburg, K., Reimanis, I.E., Kleebe, H-J., et al., 2008, Sintering kinetics of a MgAl2O4 spinel doped with LiF. *Journal of the American Ceramic Society* 91(2), 444–450. https://doi.org/10.1111/j.1551-2916.2007.02185.x.

Salem, J.A., 2013, Transparent armor ceramics as spacecraft windows. *Journal of the American Ceramic Society* 96(1), 281–289. https://doi.org/10.1111/jace.12089.

Sickafus, K., Wills, J.M., Grimes, N.W., 1999, Structure of spinel. *Journal of the American Ceramic Society* 82, 3270–3292. https://doi.org/10.1111/j.1151-2916.1999.tb02241.x.

Smart, L.E. & Moore, E.A., 2005, Solid State Chemistry An Introduction. 3rd ed. Boca Raton: Taylor & Francis Group.

Staiger, M., Bowen, P., Ketterer, J., et al., 2002, Particle size distribution measurement and assessment of agglomeration of commercial nanosized ceramic particles. *Journal of Dispersion Science and Technology* 23(5), 619–630. https://doi.org/10.1081/DIS-120015367.

Straßburger, E., 2009, Ballistic testing of transparent armour ceramics. *Journal of the European Ceramic Society* 29(2), 267–273. https://doi.org/10.1016/j.jeurceramsoc.2008.03.049.

Wang, C. & Zhao, Z., 2009, Transparent MgAl2O4 ceramic produced by spark plasma sintering. *Scripta Materialia* 61(2), 193–196.nhttps://doi.org/10.1016/j.scriptamat.2009.03.039.

Wang, X. & Atkinson, A., 2015, On the measure of ceramic fracture toughness using single edge notched beams. *Journal of the European Ceramic Society* 35(13), 3713–3720. https://doi.org/10.1016/j.jeurceramsoc.2015.05.005.